

1 INTRODUCTION

2 Above Earth's atmosphere are the Van Allen radiation belts, a toroidally-shaped
3 pair of belts that consist of a complex and dynamic plasma environment. The inner
4 radiation belt is stable, consists of mostly energetic protons, and is located within 2
5 Earth radii (measured near the equator) above Earth's surface. The outer radiation
6 belt, on the other hand, consists of mostly energetic electrons, is dynamic on hour
7 time scales, and is typically found between three and eight Earth radii above Earth's
8 surface. These belts pose a threat to space exploration due to their adverse effects on
9 our bodies and electrical components. A few effects include: a high radiation dose for
10 manned missions, degradation of silicon that causes transistor malfunction, computer
11 memory corruption due to bit flips, etc. With these effects in mind, it is no surprise
12 that the radiation belts have been extensively studied since their discovery in the
13 1960s.

14 The radiation belt particles, mostly consisting of electrons and protons, are at
15 times unstable to wave growth and generate electric and magnetic waves. These
16 waves can then accelerate and scatter radiation belt particles with a variety of wave-
17 particle mechanisms. These wave-particle interactions are believed to be responsible
18 for scattering electron microbursts, a short and intense increase of precipitating
19 electrons into Earth's atmosphere, that are capable of destroying ozone molecules
20 and rapidly deplete the outer belt's electrons.

21 Electron microbursts, henceforth referred to as microbursts, are typically
22 observed by low Earth orbiting spacecraft, sounding rockets, and high altitude
23 balloons as a sub-second impulse of electrons. Some of the most intense microbursts
24 have electron fluxes that are a factor of 10 to 100 above the background (for example
25 see Fig. 7 in Blake et al. (1996)). Since they were first reported by Anderson and

26 Milton (1964), the intense transient nature of microbursts have compelled researchers
27 to pursue an understanding of their properties, their effects on the environment, and
28 the physical mechanism(s) that create microbursts. Microbursts are widely believed
29 to be created by wave-particle scattering between a plasma wave called whistler
30 mode chorus and outer radiation belt electrons, although many details regarding the
31 scattering mechanism are unconstrained or unknown. The goal of this dissertation
32 is to expand our knowledge of the wave-particle scattering mechanism that causes
33 electron microbursts.

34 This chapter serves as an introduction to the fundamental physical concepts that
35 are essential to understand wave-particle interactions in Earth's magnetosphere. We
36 will review the main structures in the magnetosphere, review the motion of charged
37 particles in electric and magnetic fields, how particles are accelerated and lost in the
38 magnetosphere, and review the current state of our understanding of microbursts.

39 Then the rest of this dissertation expands our knowledge of microbursts. In
40 Chapter ?? (chapter numbers will be filled in the full dissertation) we will investigate
41 and model the scattering mechanism responsible for microbursts observed inside the
42 outer radiation belt, near the magnetic equator. Then in Chapters ?? and ?? we
43 will investigate the microburst scattering mechanism indirectly by estimating the
44 microburst footprint size in low Earth orbit and the magnetic equator (near where
45 microburst electrons are believed to be scattered) and compare it to sizes of chorus
46 waves estimated in prior literature.

47 Particle Populations and Their Interractions in the Magnetosphere

48 To set the scene, we will briefly tour the various macroscopic populations in the
49 magnetosphere that are most relevant to this dissertation and are illustrated in Fig.
50 1.1.

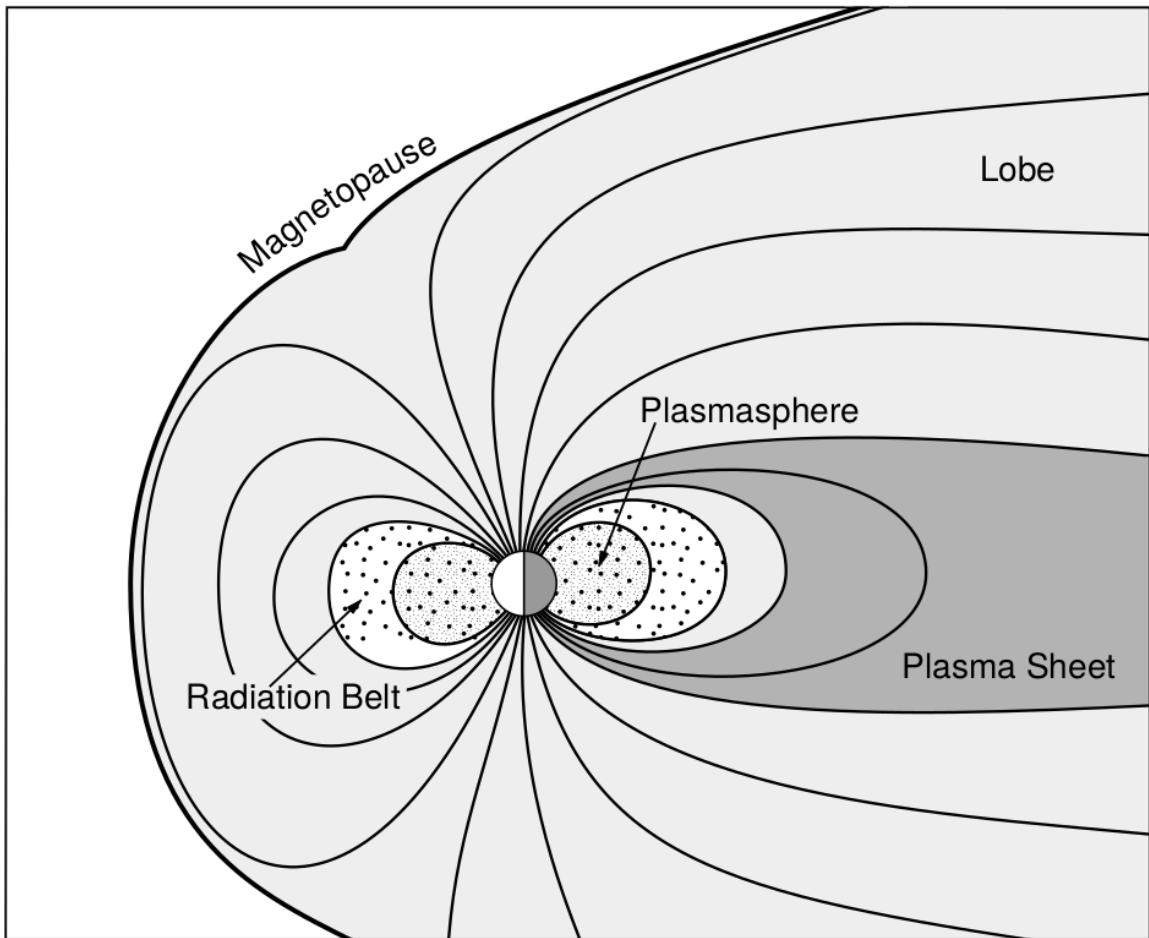


Figure 1.1: A few macroscopic structures in the magnetosphere. The magnetosphere boundary with the solar wind is the magnetopause. The magnetotail consists of two lobes that contain Earth's magnetic flux with the plasma sheet separating the two lobes. The inner magnetosphere contains the plasmasphere, the ring current, and the radiation belts which are co-located. Figure from Baumjohann and Treumann (1997).

51 The sun and its solar wind are ultimately the source of energy input into the
 52 magnetosphere. The solar wind at Earth's orbit is a plasma traveling at supersonic
 53 speeds with an embedded interplanetary magnetic field (IMF). When the solar wind
 54 encounters Earth's magnetic field, the plasma can not easily penetrate into the
 55 magnetosphere because the plasma is frozen-in on magnetic field lines. The plasma
 56 is frozen-in on magnetic field lines because plasma has a nearly infinite conductivity.
 57 Thus the plasma and its magnetic field drapes around the magnetosphere, forming a
 58 cavity in the solar wind that qualitatively has a shape as shown in Fig. 1.1. The solar
 59 wind is supersonic at 1 AU so a bow shock exists upstream of the magnetosphere
 60 which compresses and heats the solar wind. Downstream of the bow shock, the
 61 solar wind plasma flows around the magnetosphere inside the magnetosheath. The
 62 magnetopause is the surface where the solar wind ram and Earth's magnetic pressures
 63 balance. To first order, the magnetopause can be thought of as a boundary between
 64 the solar wind and Earth's magnetosphere. The shocked plasma then flows past the
 65 Earth where it shapes the magnetotail. In the magnetotail, the magnetopause exists
 66 where the solar wind magnetic pressure balances Earth's magnetic field pressure in
 67 the lobes. The magnetotail extends on the order of $100 R_E$ downstream of Earth,
 68 and the tailward stretching of magnetic field lines creates a region where Earth's
 69 Earthward and anti-Earthward magnetic fields are in proximity. In this region, the
 70 curl of \vec{B} is non-zero, thus by Ampere's law there must be a current (called the plasma
 71 sheet) near the magnetic equator (e.g. Eastwood et al., 2015).

72 Populations in the Inner Magnetosphere

73 Closer to Earth, where the magnetic field is largely dipolar, are three plasma
 74 populations that comprise the inner magnetosphere: the plasmasphere, the ring
 75 current, and the radiation belts which are shown in Fig. 1.1. Before we describe

76 these three particle populations in detail, we will introduce the coordinate system
 77 that most naturally describes the inner magnetosphere environment, and the electric
 78 fields that mostly effect low energy particles.

79 This coordinate system is shown in Fig. 1.2 and it naturally describes particles
 80 in a dipole magnetic field geometry. In this coordinate system the “radial” coordinate
 81 is the L shell. The L -shell (L) is the distance from the Earth’s center to the location
 82 where a particular magnetic field line crosses the magnetic equator, in units of
 83 Earth radii, $R_e = 6,371$ km. The azimuthal coordinate is the magnetic local time
 84 (MLT). For an observer above Earth’s north pole looking down, MLT is defined to
 85 be 0 (midnight) in the anti-sunward direction and increases in the counter-clockwise
 86 direction with 6 at dawn, 12 at noon (sunward direction), and 18 at dusk. The final
 87 coordinate is the magnetic latitude, λ , which is analogous to the latitude coordinate in
 88 the spherical coordinate system and is defined to be 0 at the magnetic equator. This
 89 coordinate system naturally describes the following inner magnetosphere populations.

90 Low energy particle dynamics in the inner magnetosphere are organized by the
 91 co-rotation and the dawn-dusk (pointing from approximately 6 to 18 MLT) electric
 92 fields. The co-rotation electric field arises from Earth’s rotation. Earth’s magnetic
 93 field and the particles frozen on it rotate with the Earth so in the magnetosphere (non-
 94 rotating) reference frame the particles appear to $\vec{E} \times \vec{B}$ drift with Earth’s rotation.
 95 Thus the co-rotation \vec{E} points towards Earth. The other electric field points from
 96 dawn to dusk is called the convection electric field and is due to the Earthward
 97 transport of particles from the magnetotail. In the magnetosphere reference frame
 98 this motion appears as an electric field pointing from dawn to dusk. The superposition
 99 of the co-rotation and and convection electric fields is a potential field shown in Fig.
 100 1.3. The shaded area in Fig. 1.3 shows where low energy electrons execute closed
 101 orbits around Earth (i.e. particles are trapped), and outside this region the particles

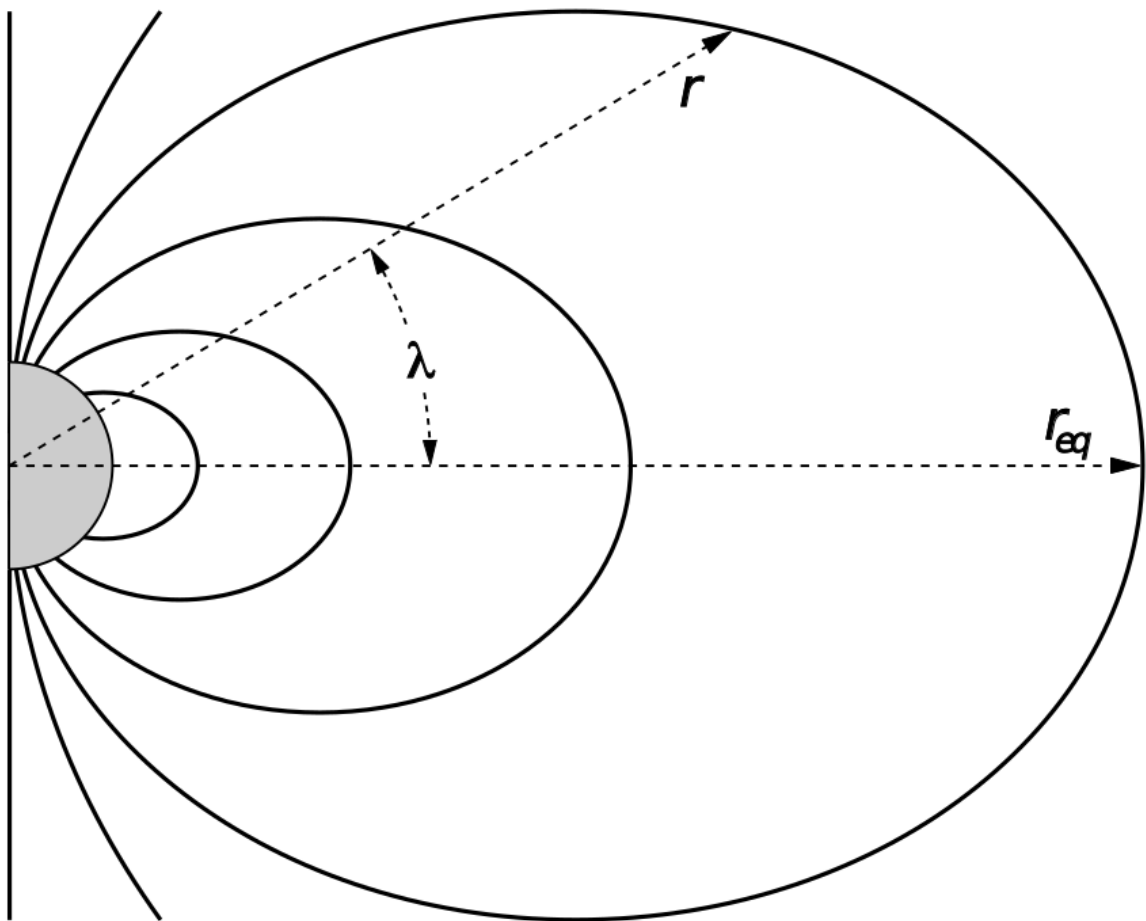


Figure 1.2: The dipole coordinate system. The magnetic latitude of \mathbf{r} is λ . The radial distance to a magnetic field line in the equatorial plane is typically given by $L = r_{eq}/R_e$. Figure from Baumjohann and Treumann (1997).

102 are not trapped. The dynamic topology of the shaded region in Fig. 1.3 is controlled
 103 by only the convection electric field which is dependent on the solar wind speed and
 104 the IMF. Due to $\vec{E} \times \vec{B}$ drift, the lowest energy particles orbit along equipotential
 105 lines in the shaded region in Fig. 1.3 and make up the plasmasphere.

106 Plasmasphere The plasmasphere is a relatively dense ($n_e \sim 10^3/\text{cm}^3$) and cool
 107 ($\sim \text{eV}$) plasma. The plasmasphere typically extends to $L \sim 4$ and the spatial extent
 108 is highly dependent on the solar wind and magnetospheric conditions. The source
 109 of the plasmasphere is the ionosphere, a layer in Earth's upper atmosphere that
 110 contains a high concentration of electrons and ions. The main mechanisms that
 111 ionize the ionosphere are ultraviolet light from the sun and particle precipitation.
 112 The ultraviolet ionization by sunlight is strongly dependent on the time of day
 113 and latitude, while particle precipitation is highly dependent on magnetospheric
 114 conditions and mostly occurs at high latitudes.

115 The outer boundary of the plasmasphere is called the plasmapause which is
 116 typically identified by a steep radial gradient in plasma density from $\sim 10^3/\text{cm}^3$ to
 117 $\sim 1/\text{cm}^3$. It is important to know the location of the plasmapause since the plasma
 118 density strongly controls the efficiency of particle scattering by waves. For example,
 119 electron scattering by chorus waves is more efficient when the ratio of the plasma and
 120 gyro frequency is low which is typically found in low plasma density regions outside
 121 of the plasmapause (e.g. Horne et al., 2003, 2005; O'Brien and Moldwin, 2003).

122 Ring Current A higher energy population is the ring current. This population
 123 consists of protons and electrons between tens and a few hundred keV that drift
 124 around the Earth. The orbits of higher energy particles are not as affected by the
 125 convection and co-rotation electric field, instead they drift around the Earth due to
 126 gradient and curvature drifts. Since the direction of the drift is dependent on charge,

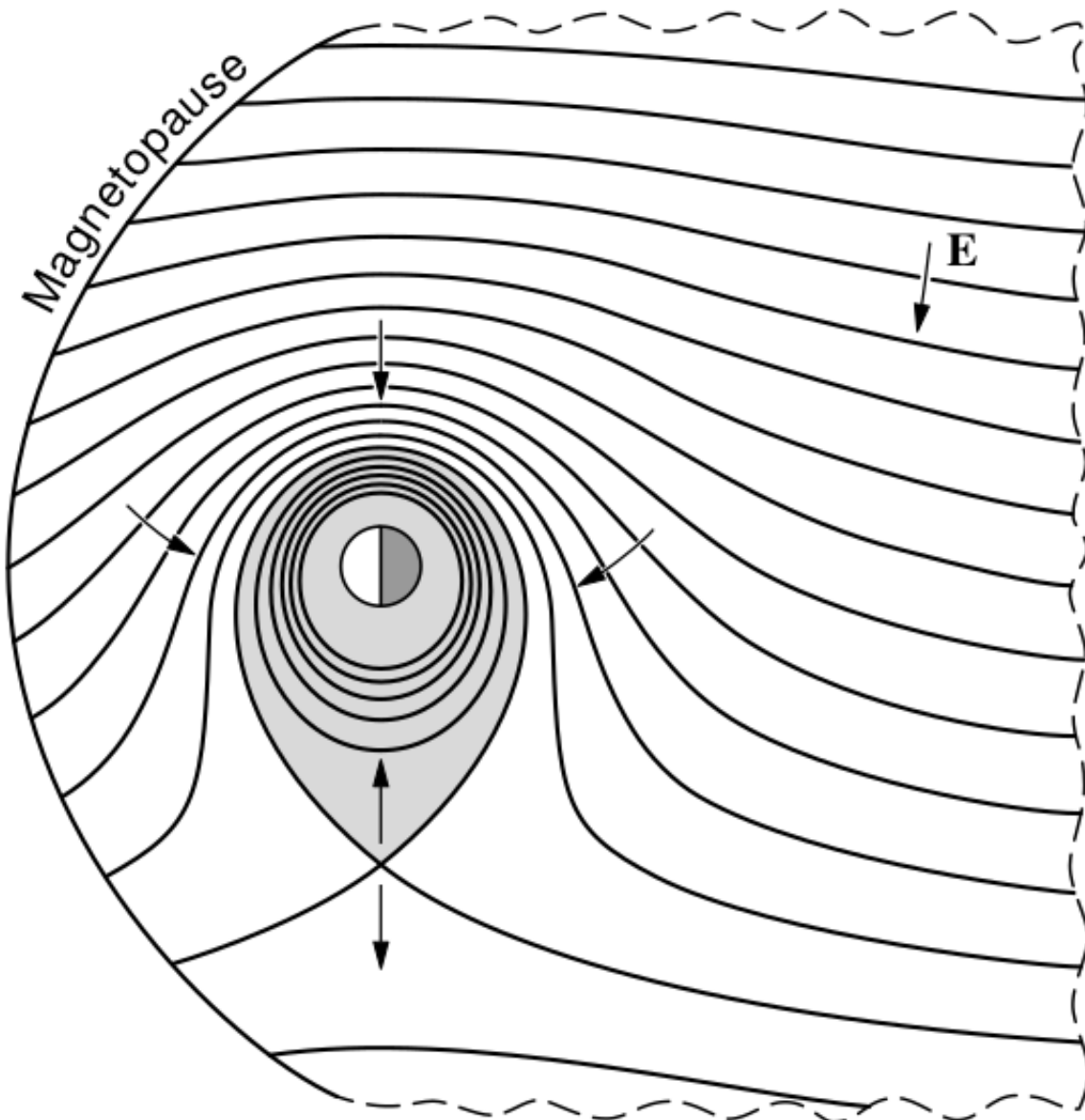


Figure 1.3: Equipotential lines and electric field arrows due to the superposition of the co-rotation and convection electric fields. Electrons in the shaded region execute closed orbits. Outside of the shaded regions the electrons are not trapped and will escape. The region separating the two regimes is called the Alfvén layer. Figure from Baumjohann and Treumann (1997).

¹²⁷ protons drift west around the Earth and electrons drift East. This effect creates a
¹²⁸ current around the Earth.

¹²⁹ The ring current generates a magnetic field which decreases the magnetic field
¹³⁰ strength at the surface of the Earth and increases it outside of the ring current. The
¹³¹ decrease of Earth's magnetic field strength is readily observed by a system of ground-
¹³² based magnetometers and is merged into a Disturbance Storm Time (DST) index
¹³³ to quantify the global reduction in the magnetic field. An example of a DST index
¹³⁴ time series from the 2015 St. Patrick's Day storm, driven by a coronal mass ejection
¹³⁵ (CME), is shown in Fig. 1.4. At the start of a storm, DST sometimes increases
¹³⁶ in response to the compression of the magnetopause by a shock wave (termed the
¹³⁷ initial phase or sudden storm commencement) and is shown by the red horizontal
¹³⁸ bar in Fig. 1.4. During the main phase of the storm the ring current population is
¹³⁹ rapidly built up and DST rapidly decreases which is shown by the green bar in Fig.
¹⁴⁰ 1.4. After the storm is over the ring current slowly recovers to pre-storm conditions
¹⁴¹ during the recovery phase shown by the blue bar in Fig. 1.4. In this phase, the
¹⁴² ring current gradually decays due to particles losses into the atmosphere, or particle
¹⁴³ transport through the magnetopause via mechanisms described later in this chapter.
¹⁴⁴ The DST index, along with other geomagnetic indices, are used by the space physics
¹⁴⁵ community to quantify the global state of the magnetosphere.

¹⁴⁶ Radiation Belts The highest particle energy populations are in the Van Allen
¹⁴⁷ radiation belts. These belts were discovered by Van Allen (1959) and Vernov and
¹⁴⁸ Chudakov (1960) during the Cold War and are a pair of toroidally shaped populations
¹⁴⁹ of trapped electrons and protons shown in Fig. 1.5. Their quiescent toroidal shape,
¹⁵⁰ similar to the shape of the plasmasphere and ring current, is a result of Earth's dipole
¹⁵¹ magnetic field.

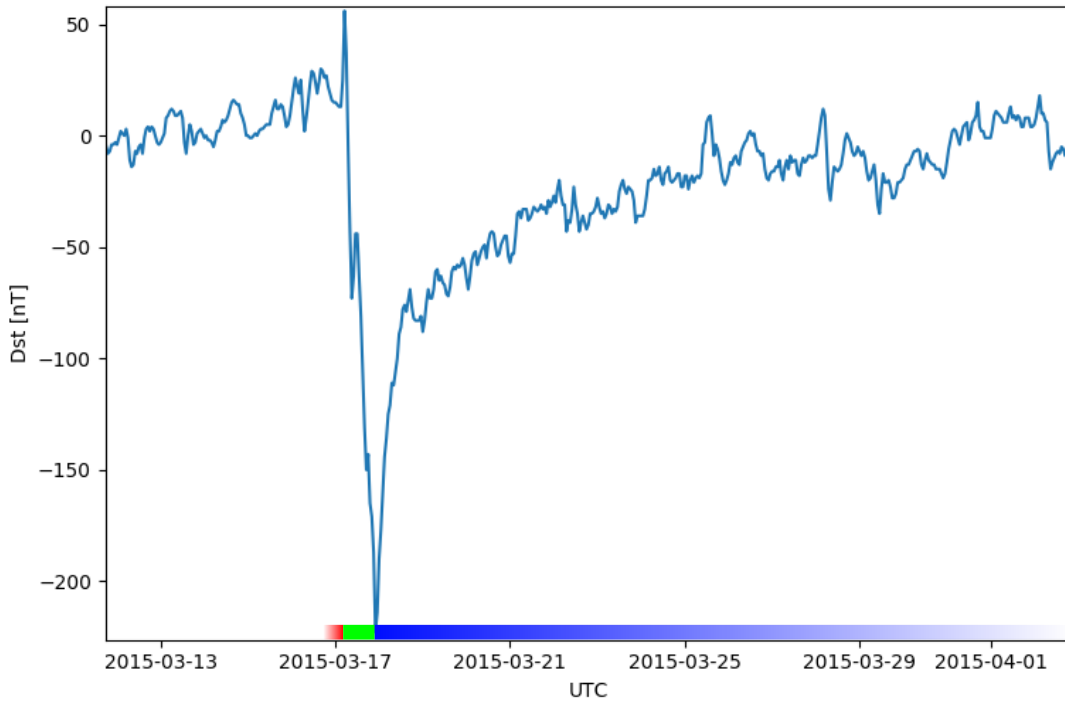


Figure 1.4: The DST index during the St. Patrick's Day 2015 storm. This storm was caused by a coronal mass ejection on March 15th, 2015. The storm phases are: initial phase, main phase, and recovery phase. The initial phase occurred when the Dst peaked at $+50$ nT on March 17th during which the ring current was eroded by the coronal mass ejection during the interval shown by the red bar shown at the bottom. Then the following rapid decrease to ≈ -200 nT was during the main phase where many injections from the magnetotail enhanced the ring current, which reduced Earth's magnetic field strength at the ground, and is shown with the green bar. Lastly, the recovery phase lasted from March 18th to approximately March 29th during which the ring current particles were lost and the ring current returned to its equilibrium state. The recovery phase is shown with the blue bar.

The Earth's Electron Radiation Belts

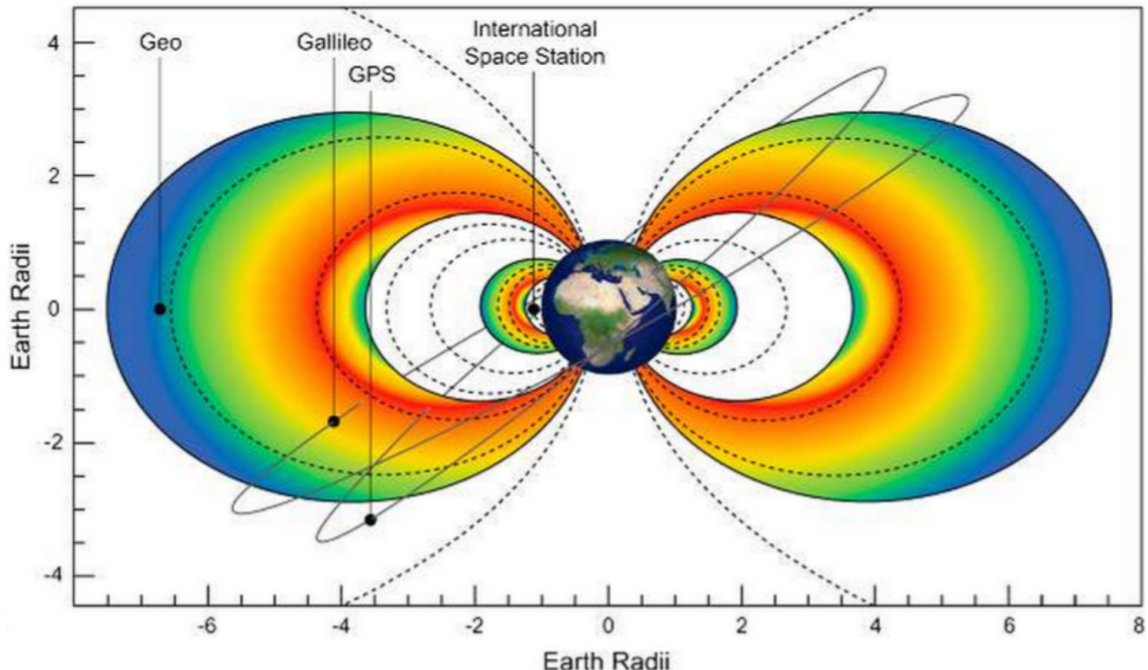


Figure 1.5: The two radiation belts with the locations of various satellites and orbits. Figure from (Horne et al., 2013).

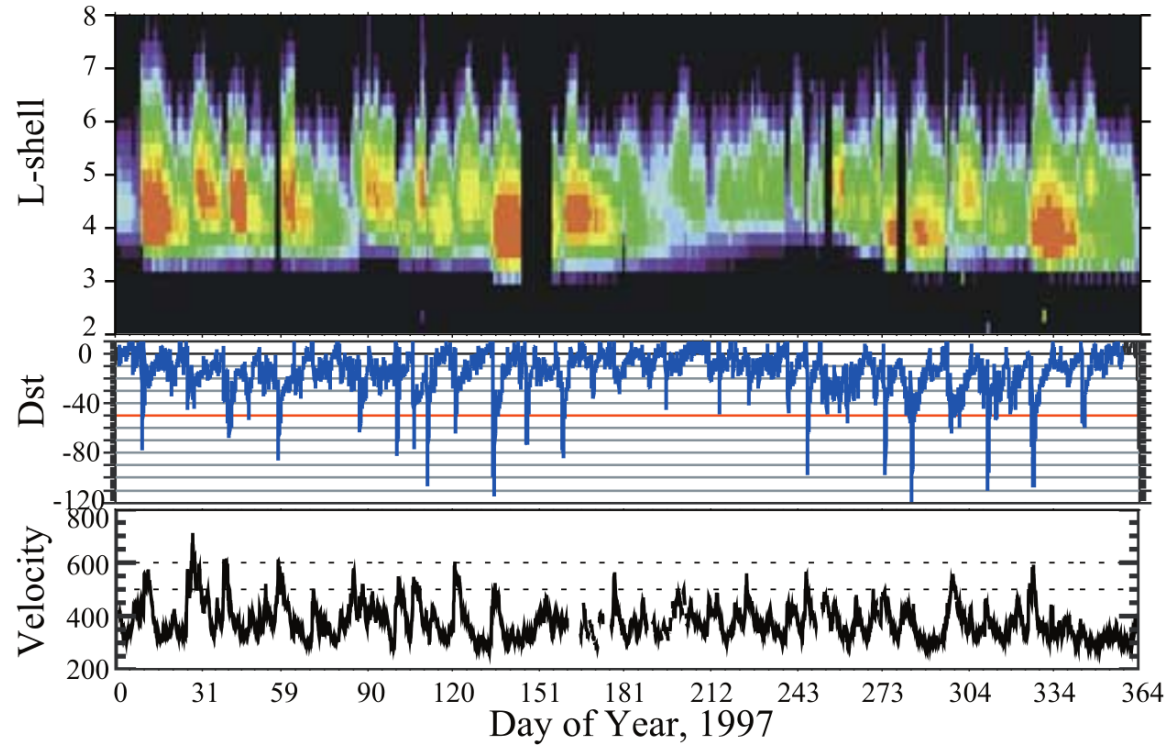


Figure 1.6: The dynamics of the outer radiation belt in 1997 from the POLAR satellite. Top panel shows the 1.2-2.4 MeV electron flux as a function of L and 1997 day of year. The middle panel shows the DST index, and bottom panel shows the solar wind velocity. Figure from (Reeves et al., 2003).

152 The inner radiation belt is extremely stable on time periods of years, extends
 153 to $L \approx 2$, and mainly consists of protons with energies between MeV and GeV and
 154 electrons with energies up to ≈ 1 MeV (Claudepierre et al., 2019). The source of
 155 inner radiation belt protons is believed to be due to cosmic-ray albedo neutron decay
 156 (e.g. Li et al., 2017) and inward radial diffusion for electrons (e.g. O'Brien et al.,
 157 2016). The gap between the inner and outer radiation belt is called the slot, which is
 158 believed to be due to hiss waves inside the plasmasphere (described below) scattering
 159 particles into the atmosphere (e.g. Breneman et al., 2015; Lyons and Thorne, 1973).

160 The outer radiation belt is much more dynamic and consists of mainly electrons
 161 of energies up to a few MeV. The outer belt's spatial extent is highly variable as
 162 shown in Fig. 1.6, and is typically observed between L of 4 and 8. The source of
 163 outer radiation belt electrons is widely believed to be injections of plasma from the
 164 magnetotail that is then accelerated to high energies.

165 Charged Particle Motion in Electric and Magnetic Fields

A charged particle trapped in the magnetosphere will experience three types of periodic motion in Earth's nearly dipolar magnetic field in the absence of electric fields. The three motions are ultimately due to the Lorentz force that a particle of momentum \vec{p} , charge q , and velocity \vec{v} experiences in an electric field \vec{E} and magnetic field \vec{B} and is given by

$$\frac{d\vec{p}}{dt} = q(\vec{E} + \vec{v} \times \vec{B}). \quad (1.1)$$

166 For many vector quantities in this dissertation, we will adopt a widely-used
 167 convention by splitting up vectors into parallel, $x_{||}$, and perpendicular, x_{\perp} components
 168 with respect to the background magnetic field. In the magnetosphere, the three
 169 periodic motions, in decreasing frequency, are gyration, bounce, and drift and are

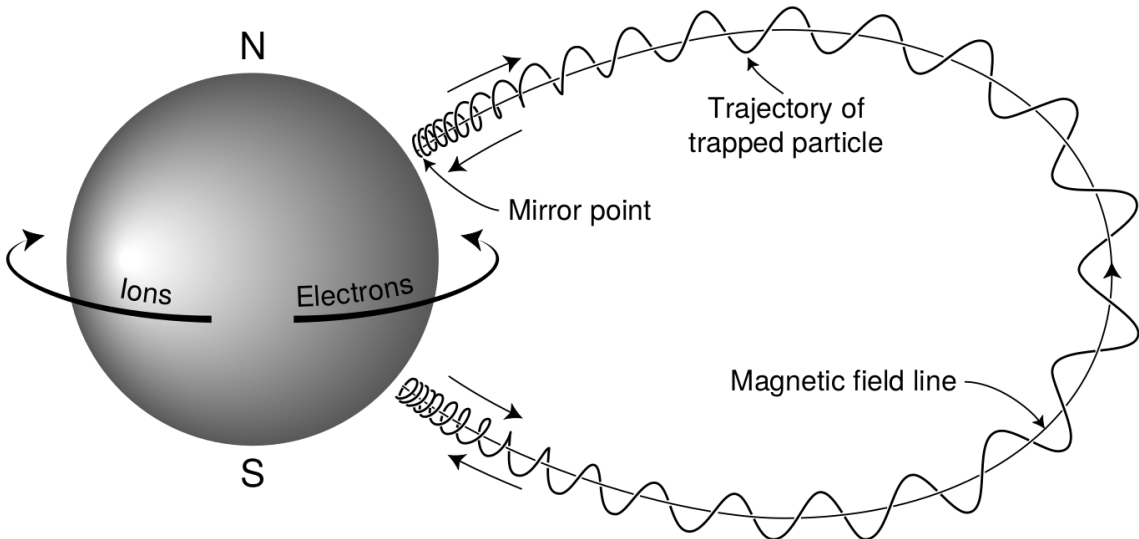


Figure 1.7: The three periodic motions of charged particles in Earth's dipole magnetic field. These motions are: gyration about the magnetic field line, bounce motion between the magnetic poles, and azimuthal drift around the Earth. Figure from (Baumjohann and Treumann, 1997).

¹⁷⁰ schematically shown in Fig. 1.7. Each periodic motion has a corresponding conserved
¹⁷¹ quantity or adiabatic invariant.

The highest frequency periodic motion is gyration about a magnetic field of magnitude B . This motion is circular with a Larmor radius of

$$r = \frac{mv_{\perp}}{|q|B} \quad (1.2)$$

where m is the mass and v_{\perp} the particle's velocity perpendicular to \vec{B} . This motion has a corresponding gyrofrequency of

$$\Omega = \frac{|q|B}{m} \quad (1.3)$$

in units of radians/second. In the radiation belts, the electron gyrofrequency, Ω_e , is on the order of a kHz near the magnetic equator. The corresponding adiabatic invariant

is found by integrating the particle's canonical momentum around the particle's path of gyration,

$$J_i = \oint (\vec{p} + q\vec{A}) \cdot d\vec{l} \quad (1.4)$$

where J_i is the i^{th} adiabatic invariant and \vec{A} is the magnetic vector potential. This integral is carried out by integrating the first term over the circumference of the gyro orbit and integrating the second term using Stokes theorem to calculate the magnetic flux enclosed by the gyro orbit. The gyration invariant is $J_1 \sim v_{\perp}^2/B$ which is conserved when the frequency, ω , of a force acting on the gyrating electron satisfies

$$\omega \ll \Omega_e.$$

The second highest frequency periodic motion is bouncing due to a parallel gradient in \vec{B} . This periodic motion naturally arises in the magnetosphere because Earth's magnetic field is stronger near the poles. To understand this motion we first we need to define the concept of pitch angle, α as the angle between \vec{B} and \vec{v} which is schematically shown in Fig. 1.8a. The pitch angle relates v with v_{\perp} and v_{\parallel} , the component of the particles velocity parallel to \vec{B} . As shown in Fig. 1.8b and 1.8c, a smaller (larger) α will increase (decrease) the distance that the charged particle travels parallel to \vec{B} during one gyration.

Assuming the particle's kinetic energy is conserved, the conservation of J_1 implies that given a particle's $v_{\perp}(0)$ and $B(0)$ at the magnetic equator (where Earth's magnetic field is usually at a minimum) we can calculate its $v_{\perp}(s)$ along the particle's path, s , by calculating $B(s)$ from magnetic field models. Thus the particle's perpendicular velocity is then related via

$$\frac{v_{\perp}^2(0)}{B(0)} = \frac{v_{\perp}^2(s)}{B(s)} \quad (1.5)$$

¹⁸⁶ which can be rewritten as

$$\frac{v^2 \sin^2 \alpha(0)}{B(0)} = \frac{v^2 - v_{||}^2(s)}{B(s)} \quad (1.6)$$

¹⁸⁷ and re-arranged to solve for $v_{||}(s)$ by

$$v_{||}(s) = v \sqrt{1 - \frac{B(s)}{B(0)} \sin^2 \alpha(0)} \quad (1.7)$$

¹⁸⁸ which will tend towards 0 as the second term in the radical approaches 1.

¹⁸⁹ The location where $v_{||}(s) = 0$ is called the mirror point and is where a particle
¹⁹⁰ stops and reverses direction. Since Earth's magnetic field is stronger towards the
¹⁹¹ poles, the mirroring particle will execute periodic bounce motion between two mirror
¹⁹² points in the northern and southern hemispheres. The corresponding adiabatic
¹⁹³ invariant, J_2 is

$$J_2 = \oint p_{||} ds \quad (1.8)$$

where ds describes the particle path between the mirror points in the northern and southern hemispheres (see Fig. 1.7). J_2 is found by substituting Eq. 1.7 into Eq. 1.8 and defining the magnetic field strength at the mirror points as B_m (where $\alpha(m) = 90^\circ$). The J_2 integral can be written as

$$J_2 = 2p \int_{m_n}^{m_s} \sqrt{1 - \frac{B(s)}{B(m)}} ds \quad (1.9)$$

¹⁹⁴ where m_n and m_s are the northern and southern mirror points, respectively. The

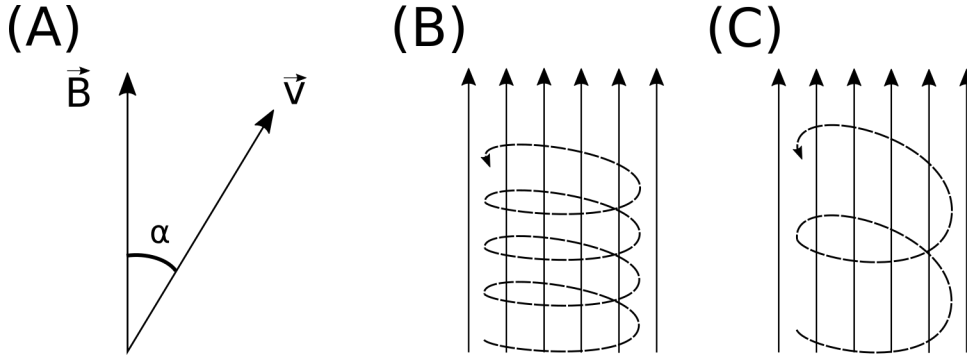


Figure 1.8: Charged particle motion in a uniform magnetic field \vec{B} . Panel (A) shows the geometry defining the pitch angle, α . Panel (B) and (C) show two helical electron trajectories with dashed lines assuming a large and small α (corresponding to a small and large parallel velocity $v_{||}$), respectively.

¹⁹⁵ bounce period can be estimated (e.g. Baumjohann and Treumann, 1997) to be

$$t_b \approx \frac{LR_e}{\sqrt{W/m}}(3.7 - 1.6 \sin \alpha(0)) \quad (1.10)$$

¹⁹⁶ where W is the particle's kinetic energy. As with gyration, the particle will bounce
¹⁹⁷ between the mirror points as long as $\omega \ll \Omega_b$, where Ω_b is the bounce frequency.

¹⁹⁸ At this stage it is instructional to introduce loss cone pitch angle, α_L .
¹⁹⁹ Conventionally, the loss cone pitch angle is defined as the pitch angle where a particle
²⁰⁰ will mirror at ≈ 100 km altitude in the atmosphere. A charged particle gyrating at
²⁰¹ those altitudes will encounter, and likely Coulomb scatter, with the dense atmosphere
²⁰² and be lost. The 100 km altitude is only a convention and not a hard boundary, e.g.
²⁰³ the peak in the 1 MeV electron ionization rate is at ≈ 60 km altitudes (Fang et al.,
²⁰⁴ 2010).

²⁰⁵ The slowest periodic motion experienced by charged particles in Earth's
²⁰⁶ magnetic field is azimuthal drift around the Earth. This drift primarily results from
²⁰⁷ a combination of a radial gradient in \vec{B} and the curvature of the magnetic field. The
²⁰⁸ radial gradient drift arises because Earth's magnetic field is stronger near the Earth.

209 The particle's gyroradius shrinks as it gyrates towards Earth, and expands when it
 210 gyrates away from Earth. The overall effect is the particle gyro orbit does not close
 211 on itself causing eastward drift of negatively charged particles and westward drift
 212 of positively charged particles. The radial gradient drift is further enhanced by the
 213 centrifugal force that a particle experiences as it bounces along the curved field lines.
 214 The drift adiabatic invariant, J_3 is found by integrating Eq. 1.4 over the complete
 215 particle orbit around the Earth. The shape of this drift orbit is known as a drift shell,
 216 and can be visualized by rotating the trapped particle trajectory in Fig. 1.7 around
 217 the axis that connects the poles. For J_3 , the first term is negligible and the second
 218 term is the magnetic flux enclosed by the drift shell, Φ_m i.e. $J_3 \sim \Phi_m$.

219 To quantify the frequencies of the three periodic motions, Fig. 1.9 from Schulz
 220 and Lanzerotti (1974) shows contours of the gyration, bounce, and drift frequencies
 221 for electrons and protons in Earth's dipole magnetic field.

Up until now we have considered the three periodic motions due Earth's magnetic field in the absence of electric fields. If there is an electric field, \vec{E} , perpendicular to \vec{B} , a particle's center of gyration (averaged position of the particle over a gyration) will drift with a velocity perpendicular to both \vec{E} and \vec{B} . The drift velocity can be solved using Eq. 1.1 and is

$$\vec{v}_E = \frac{\vec{E} \times \vec{B}}{B^2}. \quad (1.11)$$

222 If there is a parallel magnetic field, $E_{||}$, then the particle is accelerated along the
 223 magnetic field line. An $E_{||}$ pointing away from the Earth will contribute to the mirror
 224 force and raise the particle's mirror point. On the contrary, an Earthward pointing
 225 $E_{||}$ will oppose the mirror force and lower the mirror point. If the Earthward $E_{||}$
 226 lowers the mirror point into the atmosphere, those particles will precipitate into the
 227 atmosphere. This is the mechanism that generates the aurora.

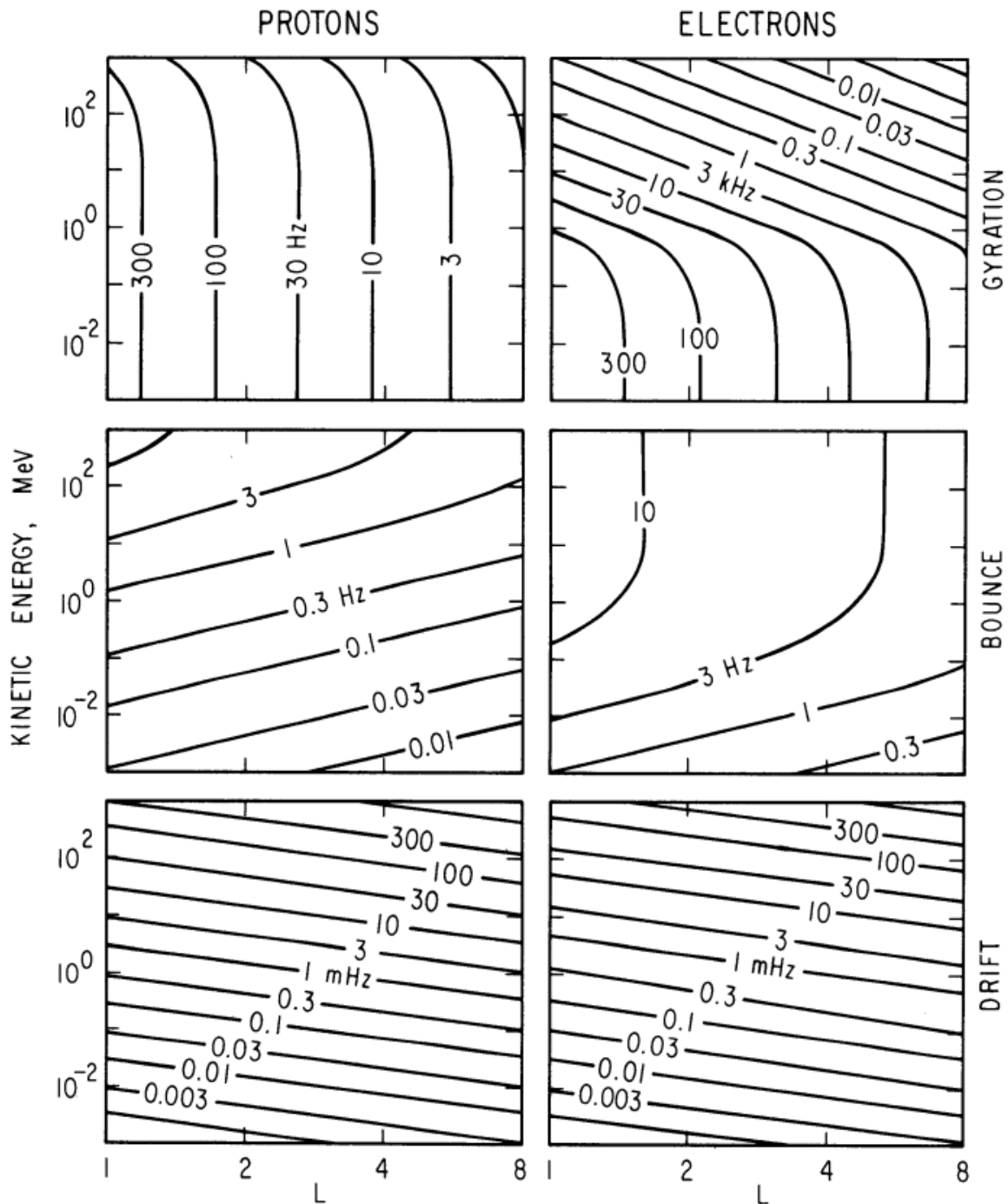


Figure 1.9: Contours of constant gyration, bounce, and drift frequencies for electrons and protons in a dipole field. Figure from Schulz and Lanzerotti (1974).

228

Radiation Belt Particle Sources and Sinks

229 Due to the highly energetic and dynamic nature of the radiation belts, and
 230 their impact on space exploration, the radiation belts have been studied for over
 231 half a century. Researchers have studied and attempted to predict the dynamics of
 232 radiation belt particles, waves, and wave-particle interactions by considering various
 233 competing particle acceleration and loss mechanisms which are described below.

234 Adiabatic Heating

One of the particle heating and transport mechanisms arises from the Earthward convection of particles. As shown in Eq. 1.5, the conservation of J_1 implies that the initial and final v_\perp depends on the change in the magnetic field magnitude. As a particle convects Earthward $B_f > B_i$ and thus v_\perp must also increase. The dipole magnetic field magnitude falls off radially as $B \sim L^{-3}$, and the change in v_\perp^2 as the particle convects towards a stronger magnetic field is

$$\frac{v_{\perp f}^2}{v_{\perp i}^2} = \left(\frac{L_i}{L_f} \right)^3 \quad (1.12)$$

235 thus the increase in $v_\perp \sim (L_i/L_f)^{3/2}$.

236 As the particle convects Earthward its $v_{||}$ also increases because the distance
 237 between the particle's mirror points decrease. Calculating the increase in $v_{||}$ is
 238 somewhat difficult, but if J_2 is conserved the increase in $v_{||}$ is approximately

$$\frac{v_{|| f}^2}{v_{|| i}^2} = \left(\frac{L_i}{L_f} \right)^k \quad (1.13)$$

239 where k ranges from 2 for equatorial pitch angles, $\alpha_{eq} = 0^\circ$, to 2.5 for $\alpha_{eq} = 90^\circ$
 240 (Baumjohann and Treumann, 1997). Since the rate of adiabatic heating is greater in

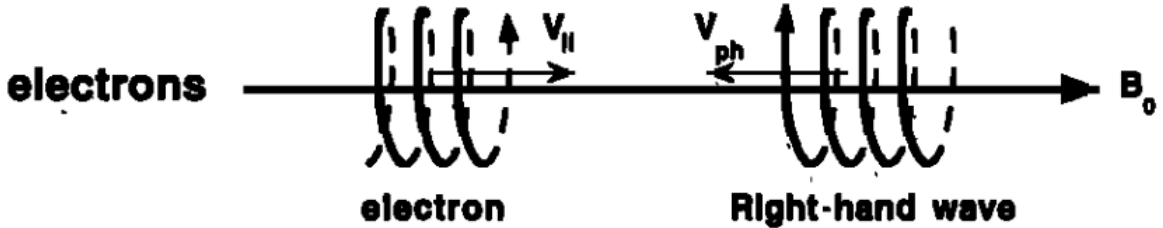
241 the perpendicular direction than heating in the parallel direction, an initially isotropic
 242 particle distribution will become anisotropic during its convection. These isotropic
 243 particles can then become unstable to wave growth and generate waves in order to
 244 reach equilibrium.

245 Wave Resonance Heating

246 Another mechanism that heats particles is caused by particles resonating with
 247 plasma waves. A few of the electromagnetic wave modes responsible for particle
 248 acceleration (and scattering) relevant to radiation belt dynamics are hiss, whistler
 249 mode chorus (chorus), and electromagnetic ion cyclotron (EMIC) waves. These waves
 250 are created by the loss cone instability that is driven by an anisotropy of electrons for
 251 chorus waves, and protons for EMIC waves. The level of anisotropy can be quantified
 252 by the ratio of the perpendicular to parallel particle temperatures (T_{\perp}/T_{\parallel}). A particle
 253 distribution is unstable when $T_{\perp}/T_{\parallel} > 1$. Since electrons gyrate in a right-handed
 254 sense, the chorus waves also tend to be right hand circularly polarized (Tsurutani and
 255 Lakhina, 1997). The same argument also applies to protons and left hand circularly
 256 polarized EMIC waves.

257 These circularly polarized waves can resonate with electrons and/or protons
 258 when their relative motion results in a static \vec{E} in the particle's reference frame. One
 259 example of a resonance between a right hand circularly polarized wave and an electron
 260 is shown in Fig. 1.10. The electron's v_{\parallel} and the wave's parallel wave vector, k_{\parallel} , are in
 261 opposite directions such that the wave frequency, ω , is Doppler shifted to an integer
 262 multiple of the Ω_e where the electron feels a static electric field and is accelerated or
 263 decelerated. Quantitatively, this resonance condition is easier to understand with the
 264 following toy model.

265 Assume a uniform magnetic field, $\vec{B} = B_0 \hat{z}$, with a parallel propagating ($k = k \hat{z}$),



$$\omega + k_{\parallel}v_{\parallel} = \Omega^-$$

Figure 1.10: The trajectories of an electron and a right-hand circularly polarized wave during a cyclotron resonance. The electron's v_{\parallel} and the wave's k_{\parallel} are in opposite directions such that the wave's frequency is Doppler shifted to an integer multiple of the electron cyclotron frequency. Figure from (Tsurutani and Lakhina, 1997).

²⁶⁶ right-hand circularly polarized wave. The wave's electric field as a function of position
²⁶⁷ and time can be written as

$$\vec{E} = E_0(\cos(\omega t - kz)\hat{x} + \sin(\omega t - kz)\hat{y}). \quad (1.14)$$

The angular component of \vec{E} that will effect the particle's v_{\perp} is

$$E_{\theta} = \vec{E} \cdot \hat{\theta} = E_0 \cos(\omega t - kz + \theta). \quad (1.15)$$

²⁶⁸ Now assume that the electron is traveling in the $-\hat{z}$ direction with a velocity, $\vec{v} =$
²⁶⁹ $-v_0\hat{z}$, so its time dependent position along \hat{z} is

$$z(t) = -v_0t \quad (1.16)$$

²⁷⁰ and gyrophase is

$$\theta(t) = -\Omega t + \theta(0) \quad (1.17)$$

²⁷¹ where the first negative sign comes from the electron's negative charge. Now we put

²⁷² this all together into Eq. 1.1 and find the force that the electron will experience is

$$m \frac{dv_\theta}{dt} = qE_\theta = qE_0 \sin((\omega + kv_0 - \Omega)t + \theta(0)). \quad (1.18)$$

²⁷³ This is a relatively complex expression, but when the time dependent component is

²⁷⁴ zero, i.e.

$$\omega + kv_0 - \Omega = 0, \quad (1.19)$$

²⁷⁵ the electron will feel a static electric field and be accelerated or decelerated depending

²⁷⁶ on θ_0 , the phase between the wave and the electron. The expression in Eq. 1.19 is

²⁷⁷ commonly referred to as the resonance condition and is more generally written as

$$\omega - k_{||}v_{||} = \frac{n\Omega_e}{\gamma} \quad (1.20)$$

²⁷⁸ where n is the resonance order, and γ is the relativistic correction (e.g. Millan and

²⁷⁹ Thorne, 2007). In the case of the cyclotron resonance ($n = 1$), the wave and cyclotron

²⁸⁰ frequencies are approximately equal and thus J_1 is violated. Since J_1 is violated, J_2

²⁸¹ and J_3 are also violated since the conditions required to violate J_2 and J_3 are less

²⁸² stringent than J_1 . It is important to remember that a particle will experience the

²⁸³ effects of many waves along its drift orbit. The typical MLT extent of a handful of

²⁸⁴ waves that are capable of resonating with radiation belt electrons are shown in Fig.

²⁸⁵ 1.11.

²⁸⁶ Particle Losses

²⁸⁷ Now that we have seen two general mechanisms with which particles are

²⁸⁸ accelerated in the magnetosphere, we will consider a few specific mechanisms that

²⁸⁹ remove particles from the magnetosphere into the atmosphere or the solar wind.

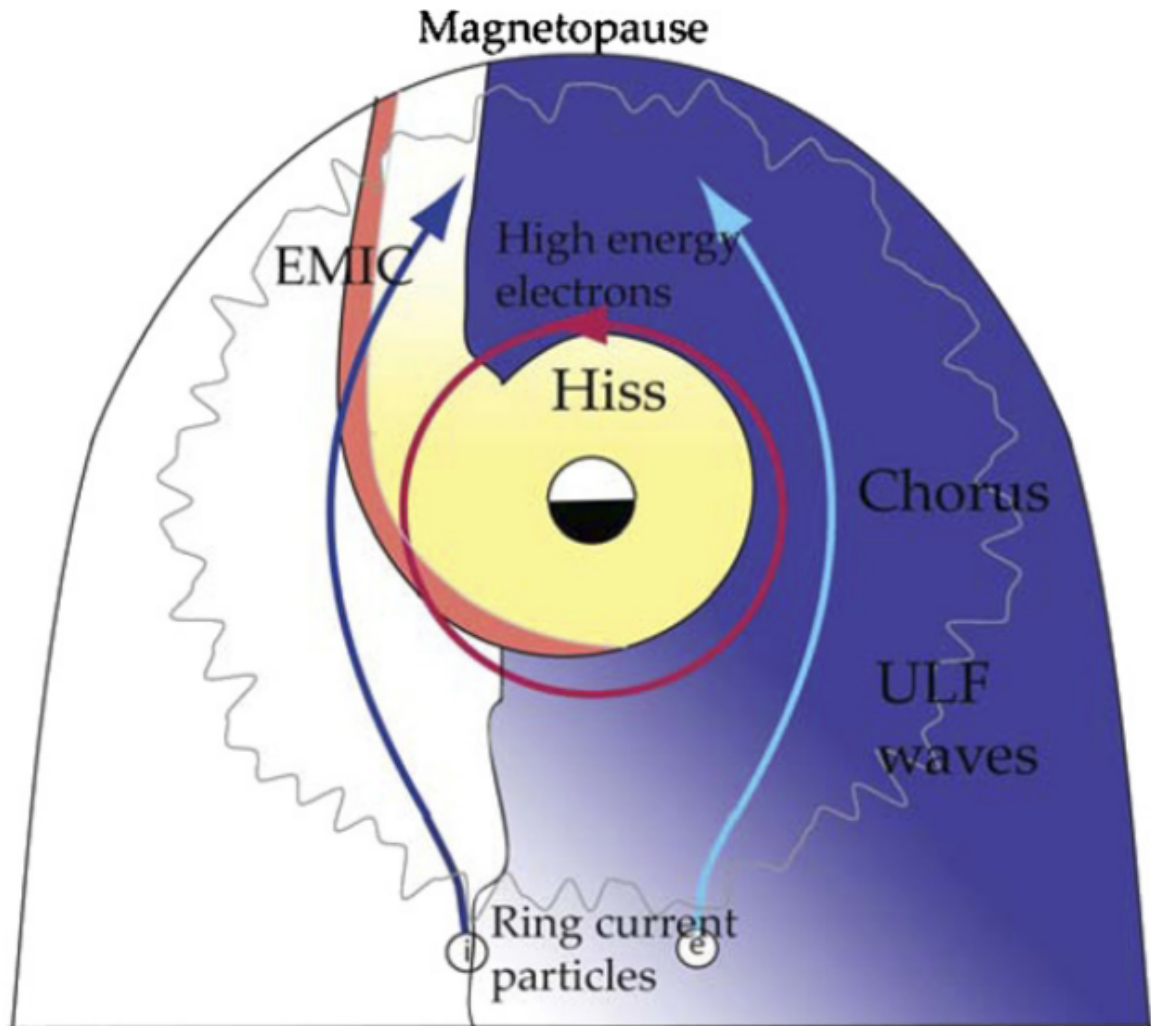


Figure 1.11: Various wave modes in the magnetosphere. Ultra low frequency waves occur through the magnetosphere. Chorus waves are typically observed in the 0-12 midnight-dawn region. EMIC waves are typically observed in the dusk MLT sector. Hiss waves are observed inside the plasmasphere. Figure from Millan and Thorne (2007).

290 One mechanism that transports magnetosperic particles into the solar wind is
 291 magnetopause shadowing (e.g. Ukhorskiy et al., 2006). Magnetopause shadowing
 292 occurs when the ring current is strengthened and Earth's magnetic field strength is
 293 increased outside of the ring current. If the ring current increases slowly enough (such
 294 that J_3 is conserved), a particle drift shell will move outward to conserve J_3 . If the
 295 particle's drift shell expands past the magnetopause, the particle will be lost to the
 296 solar wind.

297 Another particle loss (and acceleration) mechanism is called radial diffusion and
 298 is driven by ultra low frequency (ULF) modulation of Earth's magnetic field. For
 299 example, if the solar wind compresses the magnetopause on time scales shorter than
 300 the drift period, particles will experience radial diffusion. If the transport is radially
 301 inward, particles will be accelerated. On the other hand, radially outward radial
 302 diffusion can transport particles through the magnetopause where they will be lost
 303 to the solar wind. Reeves et al. (2013) investigated the driver of particle acceleration
 304 during the October 2012 storm and observationally found that inward radial diffusion
 305 was not dominant, rather local acceleration via wave-resonance heating appeared to
 306 be the dominant acceleration mechanism.

307 The loss mechanism central to this dissertation is pitch angle and energy
 308 scattering of electrons by waves. Some of the waves that scatter electrons in energy
 309 and pitch angle in the inner magnetosphere are: plasmaspheric hiss (e.g. Breneman
 310 et al., 2015; O'Brien et al., 2014), EMIC waves (e.g. Capannolo et al., 2019; Hendry
 311 et al., 2017), and chorus waves (e.g. Breneman et al., 2017; Kasahara et al., 2018;
 312 Ozaki et al., 2019). These wave-particle interactions occur when the resonance
 313 condition in Eq. 1.20 is satisfied and the particle's energy and α is modified by
 314 the wave. More details regarding the theory of pitch angle and energy diffusion is
 315 given in Chapter ???. If the wave changes α towards zero and $\alpha < \alpha_L$, then the

³¹⁶ particle's mirror point dips below 100 km altitude where the particle can be lost from
³¹⁷ the magnetosphere. One manifestation of pitch angle scattering of particles into the
³¹⁸ loss cone are microbursts, a sub-second duration impulse of electrons.

319

Microbursts

³²⁰ Microbursts were first seen with high altitude balloons which measured bremsstrahlung
³²¹ X-rays emitted by microburst electrons impacting the atmosphere by Anderson
³²² and Milton (1964). In the following years, numerous balloon flights expanded our
³²³ knowledge of non-relativistic (< 500 keV) microbursts by quantifying the microburst
³²⁴ spatial extent, temporal width, occurrence frequency, extent in L and MLT, and
³²⁵ their source. It is worth noting that relativistic microbursts have not yet been
³²⁶ observed by high altitude balloons. The microburst source was initially believed to be
³²⁷ either a local plasma instability or a propagating disturbance in the magnetosphere
³²⁸ (Barcus et al., 1966; Brown et al., 1965; Parks, 1967; Trefall et al., 1966). Soon after,
³²⁹ both non-relativistic and relativistic microburst electrons were directly observed in
³³⁰ LEO with spacecraft including the Solar Anomalous and Magnetospheric Particle
³³¹ Explorer (SAMPEX) (e.g. Blake et al., 1996; Blum et al., 2015; Douma et al., 2019,
³³² 2017; Greeley et al., 2019; Lorentzen et al., 2001a,b; Nakamura et al., 1995, 2000;
³³³ O'Brien et al., 2004, 2003), Montana State University's (MSU) Focused Investigation
³³⁴ of Relativistic Electron Bursts: Intensity, Range, and Dynamics II (FIREBIRD-II)
³³⁵ (Anderson et al., 2017; Breneman et al., 2017; Crew et al., 2016; Klumpar et al.,
³³⁶ 2015; Spence et al., 2012), and Science Technologies Satellite (STSAT-I) (e.g. Lee
³³⁷ et al., 2012, 2005). An example microburst time series is shown in Fig. 1.12 and was
³³⁸ observed by the FIREBIRD-II CubeSats. The prominent features of the example
³³⁹ microbursts in Fig. 1.12 are their sub-second duration, half order of magnitude
³⁴⁰ increase in count rate above the falling background, and their 200-800 keV energy

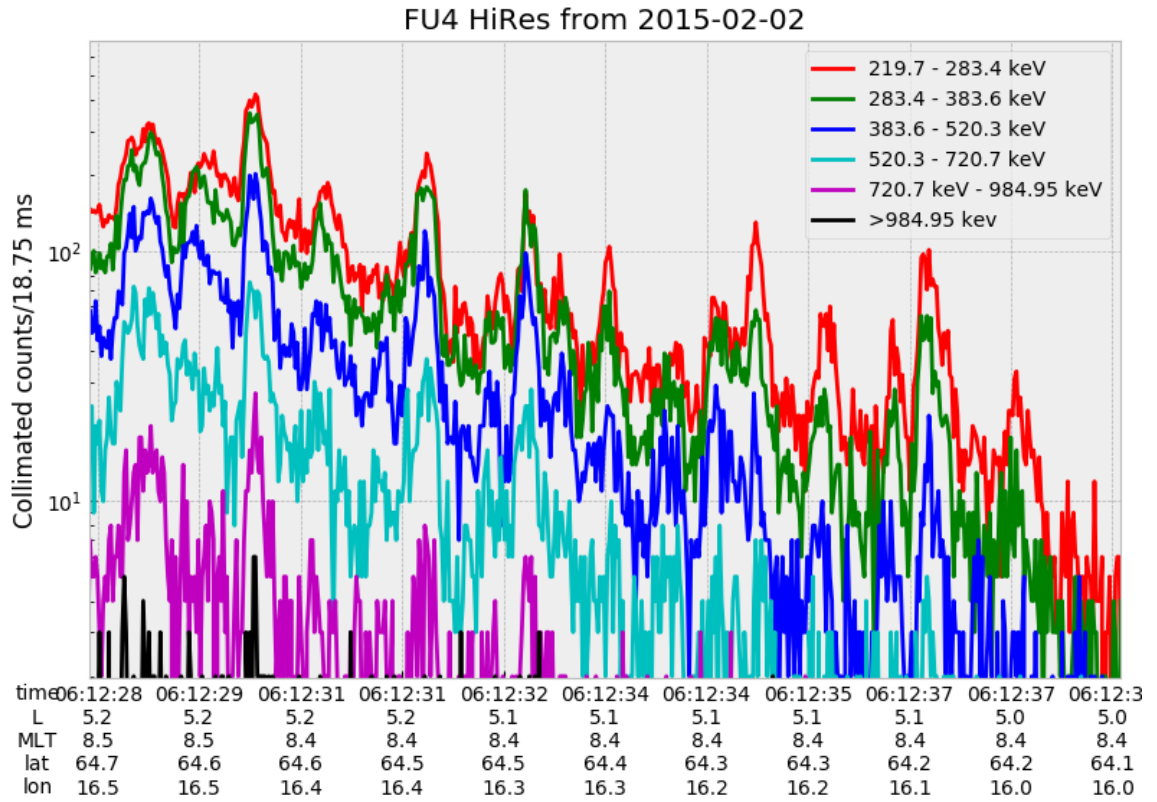


Figure 1.12: An example train of microbursts observed by FIREBIRD-II unit 4 on February 2nd, 2015. The colored curves show the differential energy channel count rates in five channels from ≈ 200 keV to 1 MeV and a sixth integral energy channel with a 1 MeV threshold. The x-axis labels show auxiliary information such as time of observation and the spacecraft position in L, MLT, latitude and longitude coordinates.

³⁴¹ extent.

³⁴² Microbursts are observed on magnetic field footprints that are connected to the
³⁴³ outer radiation belt (approximately $4 < L < 8$). They are predominately observed in
³⁴⁴ the 0-12 MLT sector with an elevated occurrence frequency during magnetospherically
³⁴⁵ disturbed times as shown in Fig. 1.13 (e.g. Douma et al., 2017). O'Brien et al. (2003)
³⁴⁶ used SAMPEX relativistic electron data and found that microbursts predominately
³⁴⁷ occur during the main phase of storms, with a heightened occurrence rate during the

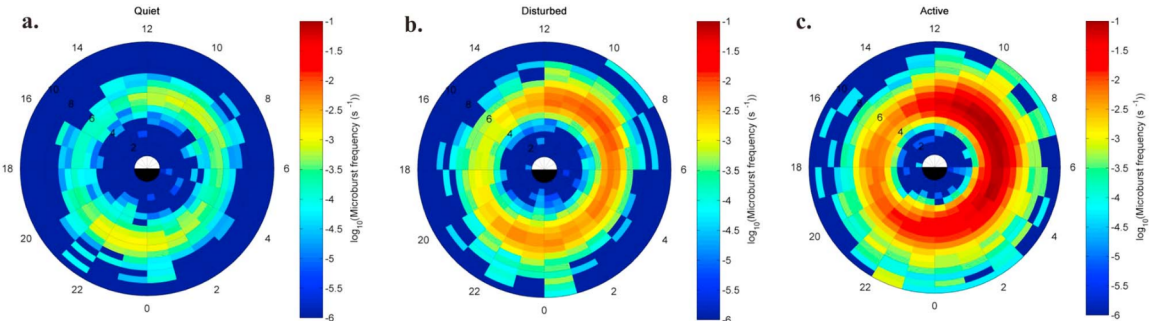


Figure 1.13: Distribution of > 1 MeV microburst occurrence rates as a function of L and MLT. The three panels show the microburst occurrence rate dependence on geomagnetic activity, parameterized by the auroral electrojet (AE) index for (a) $AE < 100$ nT, (b) $100 < AE < 300$ nT and (c) $AE > 300$ nT. Figure from Douma et al. (2017).

348 recovery phase. Microburst occurrence rates are also higher during high solar wind
 349 velocity events e.g. from co-rotating interaction regions (Greeley et al., 2019; O'Brien
 350 et al., 2003).

351 The estimated impact of microbursts on the atmosphere and the radiation
 352 belts is significant. Relativistic microburst electrons impacting the atmosphere are
 353 ionized at < 100 km altitudes, with higher energy electrons penetrating closer to
 354 the surface. The resulting chemical reaction of microburst electrons impacting the
 355 atmosphere produces odd hydrogen HO_x and odd nitrogen NO_x molecules, which
 356 are partially responsible for destroying ozone (O_3). Seppälä et al. (2018) modeled
 357 a six hour relativistic microburst storm and found that the mesospheric ozone was
 358 reduced by 7 – 12% in the summer months and 12 – 20% in the winter months, so
 359 microbursts may have a non-negligible contribution to the dynamics of atmospheric
 360 ozone. Furthermore, microbursts have also been estimated to have a significant
 361 impact on the outer radiation belt electron population. The loss of all radiation
 362 belt electrons due to microbursts have been estimated to be on the order of a day
 363 (Breneman et al., 2017; Douma et al., 2019; Lorentzen et al., 2001b; O'Brien et al.,

³⁶⁴ 2004; Thorne et al., 2005).

³⁶⁵ The wave-particle interactions responsible for generating microbursts are also
³⁶⁶ believed to accelerate electrons in the radiation belts. As mentioned earlier, when
³⁶⁷ an electron is in resonance with a wave, energy is exchanged with the wave and
³⁶⁸ the electron is either accelerated or decelerated. The signature of wave-particle
³⁶⁹ acceleration been observed for radiation belt electrons (e.g. Horne et al., 2005;
³⁷⁰ Meredith et al., 2002; Reeves et al., 2013), and O'Brien et al. (2003) presented evidence
³⁷¹ that enhancements in chorus waves, microbursts, and radiation belt electrons are
³⁷² related. To explain their observations, O'Brien et al. (2003) proposed that microburst
³⁷³ precipitation is a side effect of electron acceleration due to chorus waves.

³⁷⁴ The widely used theoretical framework to model the wave-particle interactions
³⁷⁵ responsible for accelerating electrons and scattering microbursts is quasi-linear
³⁷⁶ diffusion (e.g. Horne et al., 2005; Meredith et al., 2002; Summers, 2005; Summers
³⁷⁷ et al., 1998; Thorne et al., 2005; Walker, 1993). This framework is explained in
³⁷⁸ Chapter ??, and applied to an observation of a microburst in the heart of the
³⁷⁹ radiation belt. Qualitatively, when a particle is resonant with a wave it can either
³⁸⁰ be transported in pitch angle towards the loss cone and lose energy to the wave, or
³⁸¹ transported away from the loss cone and gain energy from the wave.

³⁸² As previously mentioned, the range of observed microburst energies range from a
³⁸³ few tens of keV (e.g Datta et al., 1997; Parks, 1967) to greater than 1 MeV (e.g. Blake
³⁸⁴ et al., 1996; Greeley et al., 2019). The microburst electron flux (J) falls off in energy,
³⁸⁵ and the microburst energy spectra is typically well fit to a decaying exponential

$$J(E) = J_0 e^{-E/E_0} \quad (1.21)$$

³⁸⁶ where J_0 is the flux at 0 keV (unphysical free parameter) and E_0 quantifies the

efficiency of the scattering mechanism in energy (e.g. Datta et al., 1997; Lee et al., 2005; Parks, 1967). A small E_0 suggests that mostly low energy particles are scattered. In contrast a high E_0 suggests that the scattering mechanism scatters low and high energy electrons. Reality is a bit more messy and a high E_0 may be a signature of a scattering mechanism that is most efficient at scattering high energy electrons, with a relatively minor efficiency to scatter low energy electrons. Since there are many more low energy electrons available to scatter, there may be relatively more low energy electrons scattered.

The short microburst duration, as observed by a single LEO satellite in a highly inclined orbit (motion is mostly latitudinal), has an ambiguity when interpreting what is a microburst. The two possible realities are: a microburst is very narrow in latitude and persistent, or transient. There are a few ways to distinguish between the two possible realities, and each one has a unique set of advantages.

A high altitude balloon essentially provides a stationary view of the precipitating particles under the radiation belt footprints. An intense transient microburst can be unambiguously identified above the slowly varying background. On the other hand, if the microburst precipitation is stationary, there will be too little contrast between the microburst and the background fluxes to be found.

Multi-spacecraft missions provide an alternate solution that can determine if a microburst is a spatial or a transient phenomena. As is illustrated in Fig. 1.14, a transient microburst can be recognized if both spacecraft simultaneously observe it. The size of the microburst footprint must then be larger than the spacecraft separation. On the contrary, if two spacecraft observe a microburst-like feature at the same location but at different times, then the feature is stationary and may be a curtain (Blake and O'Brien, 2016). Both balloon and multi-spacecraft observational methods have a unique set of strengths. This dissertation takes the multi-spacecraft

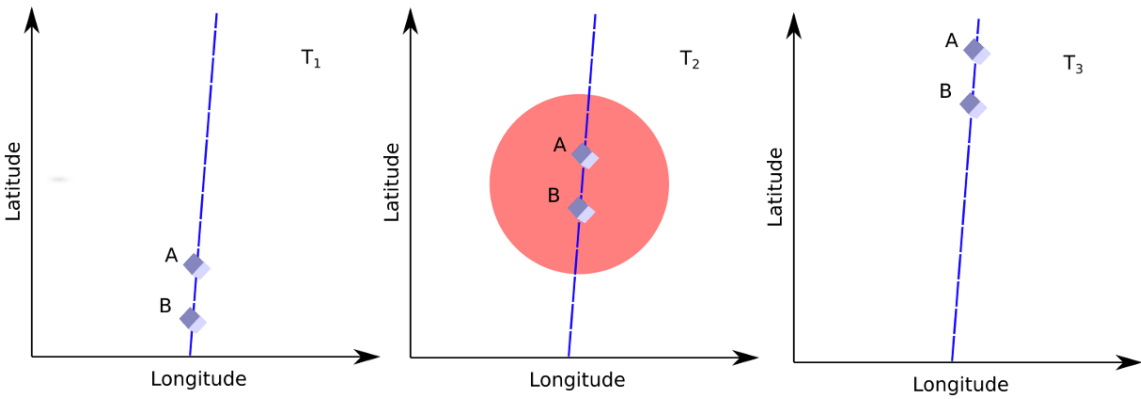


Figure 1.14: Three snapshots of a temporal microburst observed simultaneously by a pair of polar-orbiting spacecraft. The spacecraft are identified by labels "A" and "B" and are traveling upwards on the blue dashed orbital track. At T_1 the spacecraft are traveling upwards and no microburst is observed. Then at T_2 both spacecraft simultaneously observe a microburst shown by the red circle. In the last snapshot, T_3 , the microburst has precipitated and no longer observed by the spacecraft.

⁴¹³ approach to identify and study microbursts.

⁴¹⁴

Scope of Research

⁴¹⁵ This dissertation furthers our understanding of the microburst scattering
⁴¹⁶ mechanism by presenting observational evidence of microburst scattering directly,
⁴¹⁷ and measuring microburst sizes and comparing them to the size of chorus waves.
⁴¹⁸ Chapter ?? describes a microburst scattering event observed by NASA's Van Allen
⁴¹⁹ Probes. For this event, particle and wave measurements were analyzed and modeled
⁴²⁰ in the theoretical framework of pitch angle and energy diffusion. The following two
⁴²¹ chapters present studies of microburst sizes in comparison to chorus waves. Chapter
⁴²² ?? describes a bouncing packet microburst observation made by the FIREBIRD-II
⁴²³ mission where the microburst's lower bound longitudinal and latitudinal sizes were
⁴²⁴ estimated. Chapter ?? expands the case study from Chapter ?? to a statistical study
⁴²⁵ of microburst sizes using The Aerospace Corporation's AeroCube-6 (AC6) CubeSats.

⁴²⁶ In this study, a Monte Carlo and analytic microburst size models were developed
⁴²⁷ to account for the compounding statistical effects of random microburst sizes and
⁴²⁸ locations. Lastly, Chapter ?? will summarize this work and make concluding remarks
⁴²⁹ regarding outstanding questions in microburst physics.

- 431 Anderson, B., Shekhar, S., Millan, R., Crew, A., Spence, H., Klumpar, D., Blake, J.,
 432 O'Brien, T., and Turner, D. (2017). Spatial scale and duration of one microburst
 433 region on 13 August 2015. *Journal of Geophysical Research: Space Physics*.
- 434 Anderson, K. A. and Milton, D. W. (1964). Balloon observations of X rays in the
 435 auroral zone: 3. High time resolution studies. *Journal of Geophysical Research*,
 436 69(21):4457–4479.
- 437 Barcus, J., Brown, R., and Rosenberg, T. (1966). Spatial and temporal character of
 438 fast variations in auroral-zone x rays. *Journal of Geophysical Research*, 71(1):125–
 439 141.
- 440 Baumjohann, W. and Treumann, R. A. (1997). *Basic space plasma physics*. World
 441 Scientific.
- 442 Blake, J.,Looper, M., Baker, D., Nakamura, R., Klecker, B., and Hovestadt, D.
 443 (1996). New high temporal and spatial resolution measurements by sampex of the
 444 precipitation of relativistic electrons. *Advances in Space Research*, 18(8):171 – 186.
- 445 Blake, J. B. and O'Brien, T. P. (2016). Observations of small-scale latitudinal
 446 structure in energetic electron precipitation. *Journal of Geophysical Research: Space
 447 Physics*, 121(4):3031–3035. 2015JA021815.
- 448 Blum, L., Li, X., and Denton, M. (2015). Rapid MeV electron precipitation as
 449 observed by SAMPEX/HILT during high-speed stream-driven storms. *Journal of
 450 Geophysical Research: Space Physics*, 120(5):3783–3794. 2014JA020633.
- 451 Breneman, A., Crew, A., Sample, J., Klumpar, D., Johnson, A., Agapitov, O.,
 452 Shumko, M., Turner, D., Santolik, O., Wygant, J., et al. (2017). Observations
 453 directly linking relativistic electron microbursts to whistler mode chorus: Van allen
 454 probes and FIREBIRD II. *Geophysical Research Letters*.
- 455 Breneman, A. W., Halford, A., Millan, R., McCarthy, M., Fennell, J., Sample, J.,
 456 Woodger, L., Hospodarsky, G., Wygant, J. R., Cattell, C. A., et al. (2015). Global-
 457 scale coherence modulation of radiation-belt electron loss from plasmaspheric hiss.
 458 *Nature*, 523(7559):193.
- 459 Brown, R., Barcus, J., and Parsons, N. (1965). Balloon observations of auroral zone
 460 x rays in conjugate regions. 2. microbursts and pulsations. *Journal of Geophysical
 461 Research (U.S.)*.
- 462 Capannolo, L., Li, W., Ma, Q., Shen, X.-C., Zhang, X.-J., Redmon, R., Rodriguez,
 463 J., Engebretson, M., Kletzing, C., Kurth, W., et al. (2019). Energetic electron
 464 precipitation: multi-event analysis of its spatial extent during emic wave activity.
 465 *Journal of Geophysical Research: Space Physics*.

- 466 Claudepierre, S., O'Brien, T.,Looper, M., Blake, J., Fennell, J., Roeder, J.,
 467 Clemmons, J., Mazur, J., Turner, D., Reeves, G., et al. (2019). A revised look
 468 at relativistic electrons in the earth's inner radiation zone and slot region. *Journal
 469 of Geophysical Research: Space Physics*, 124(2):934–951.
- 470 Crew, A. B., Spence, H. E., Blake, J. B., Klumpar, D. M., Larsen, B. A., O'Brien,
 471 Driscoll, S., Handley, M., Legere, J., Longworth, S., Mashburn, K.,
 472 Mosleh, E., Ryhajlo, N., Smith, S., Springer, L., and Widholm, M. (2016). First
 473 multipoint in situ observations of electron microbursts: Initial results from the
 474 NSF FIREBIRD II mission. *Journal of Geophysical Research: Space Physics*,
 475 121(6):5272–5283. 2016JA022485.
- 476 Datta, S., Skoug, R., McCarthy, M., and Parks, G. (1997). Modeling of microburst
 477 electron precipitation using pitch angle diffusion theory. *Journal of Geophysical
 478 Research: Space Physics*, 102(A8):17325–17333.
- 479 Douma, E., Rodger, C., Blum, L., O'Brien, T., Clilverd, M., and Blake, J. (2019).
 480 Characteristics of relativistic microburst intensity from sampex observations.
 481 *Journal of Geophysical Research: Space Physics*.
- 482 Douma, E., Rodger, C. J., Blum, L. W., and Clilverd, M. A. (2017). Occurrence
 483 characteristics of relativistic electron microbursts from SAMPEX observations.
 484 *Journal of Geophysical Research: Space Physics*, 122(8):8096–8107. 2017JA024067.
- 485 Eastwood, J., Hietala, H., Toth, G., Phan, T., and Fujimoto, M. (2015). What
 486 controls the structure and dynamics of earths magnetosphere? *Space Science
 487 Reviews*, 188(1-4):251–286.
- 488 Fang, X., Randall, C. E., Lummerzheim, D., Wang, W., Lu, G., Solomon, S. C., and
 489 Frahm, R. A. (2010). Parameterization of monoenergetic electron impact ionization.
 490 *Geophysical Research Letters*, 37(22).
- 491 Greeley, A., Kanekal, S., Baker, D., Klecker, B., and Schiller, Q. (2019). Quantifying
 492 the contribution of microbursts to global electron loss in the radiation belts. *Journal
 493 of Geophysical Research: Space Physics*.
- 494 Hendry, A. T., Rodger, C. J., and Clilverd, M. A. (2017). Evidence of sub-mev
 495 emic-driven electron precipitation. *Geophysical Research Letters*, 44(3):1210–1218.
- 496 Horne, R., Glauert, S., Meredith, N., Boscher, D., Maget, V., Heynderickx, D., and
 497 Pitchford, D. (2013). Space weather impacts on satellites and forecasting the earth's
 498 electron radiation belts with spacecast. *Space Weather*, 11(4):169–186.
- 499 Horne, R., Glauert, S., and Thorne, R. (2003). Resonant diffusion of radiation belt
 500 electrons by whistler-mode chorus. *Geophysical research letters*, 30(9).

- 501 Horne, R. B., Thorne, R. M., Shprits, Y. Y., Meredith, N. P., Glauert, S. A., Smith,
 502 A. J., Kanekal, S. G., Baker, D. N., Engebretson, M. J., Posch, J. L., et al.
 503 (2005). Wave acceleration of electrons in the van allen radiation belts. *Nature*,
 504 437(7056):227.
- 505 Kasahara, S., Miyoshi, Y., Yokota, S., Mitani, T., Kasahara, Y., Matsuda, S.,
 506 Kumamoto, A., Matsuoka, A., Kazama, Y., Frey, H., et al. (2018). Pulsating
 507 aurora from electron scattering by chorus waves. *Nature*, 554(7692):337.
- 508 Klumpar, D., Springer, L., Mosleh, E., Mashburn, K., Berardinelli, S., Gunderson,
 509 A., Handly, M., Ryhajlo, N., Spence, H., Smith, S., Legere, J., Widholm, M.,
 510 Longworth, S., Crew, A., Larsen, B., Blake, J., and Walmsley, N. (2015). Flight
 511 system technologies enabling the twin-cubesat firebird-ii scientific mission.
- 512 Lee, J. J., Parks, G. K., Lee, E., Tsurutani, B. T., Hwang, J., Cho, K. S., Kim, K.-H.,
 513 Park, Y. D., Min, K. W., and McCarthy, M. P. (2012). Anisotropic pitch angle
 514 distribution of 100 keV microburst electrons in the loss cone: measurements from
 515 STSAT-1. *Annales Geophysicae*, 30(11):1567–1573.
- 516 Lee, J.-J., Parks, G. K., Min, K. W., Kim, H. J., Park, J., Hwang, J., McCarthy,
 517 M. P., Lee, E., Ryu, K. S., Lim, J. T., Sim, E. S., Lee, H. W., Kang, K. I., and
 518 Park, H. Y. (2005). Energy spectra of 170–360 keV electron microbursts measured
 519 by the korean STSAT-1. *Geophysical Research Letters*, 32(13). L13106.
- 520 Li, X., Selesnick, R., Schiller, Q., Zhang, K., Zhao, H., Baker, D. N., and Temerin,
 521 M. A. (2017). Measurement of electrons from albedo neutron decay and neutron
 522 density in near-earth space. *Nature*, 552(7685):382.
- 523 Lorentzen, K. R., Blake, J. B., Inan, U. S., and Bortnik, J. (2001a). Observations
 524 of relativistic electron microbursts in association with VLF chorus. *Journal of
 525 Geophysical Research: Space Physics*, 106(A4):6017–6027.
- 526 Lorentzen, K. R., Looper, M. D., and Blake, J. B. (2001b). Relativistic electron
 527 microbursts during the GEM storms. *Geophysical Research Letters*, 28(13):2573–
 528 2576.
- 529 Lyons, L. R. and Thorne, R. M. (1973). Equilibrium structure of radiation belt
 530 electrons. *Journal of Geophysical Research*, 78(13):2142–2149.
- 531 Meredith, N., Horne, R., Summers, D., Thorne, R., Iles, R., Heynderickx, D., and
 532 Anderson, R. (2002). Evidence for acceleration of outer zone electrons to relativistic
 533 energies by whistler mode chorus. In *Annales Geophysicae*, volume 20, pages 967–
 534 979.
- 535 Millan, R. and Thorne, R. (2007). Review of radiation belt relativistic electron losses.
 536 *Journal of Atmospheric and Solar-Terrestrial Physics*, 69(3):362 – 377.

- 537 Nakamura, R., Baker, D. N., Blake, J. B., Kanekal, S., Klecker, B., and Hovestadt,
 538 D. (1995). Relativistic electron precipitation enhancements near the outer edge of
 539 the radiation belt. *Geophysical Research Letters*, 22(9):1129–1132.
- 540 Nakamura, R., Isowa, M., Kamide, Y., Baker, D., Blake, J., and Looper, M. (2000).
 541 Observations of relativistic electron microbursts in association with VLF chorus.
 542 *J. Geophys. Res.*, 105:15875–15885.
- 543 O'Brien, T., Claudepierre, S., Blake, J., Fennell, J. F., Clemmons, J., Roeder, J.,
 544 Spence, H. E., Reeves, G., and Baker, D. (2014). An empirically observed pitch-
 545 angle diffusion eigenmode in the earth's electron belt near $l^*= 5.0$. *Geophysical*
 546 *Research Letters*, 41(2):251–258.
- 547 O'Brien, T., Claudepierre, S., Guild, T., Fennell, J., Turner, D., Blake, J., Clemmons,
 548 J., and Roeder, J. (2016). Inner zone and slot electron radial diffusion revisited.
 549 *Geophysical Research Letters*, 43(14):7301–7310.
- 550 O'Brien, T. and Moldwin, M. (2003). Empirical plasmapause models from magnetic
 551 indices. *Geophysical Research Letters*, 30(4).
- 552 O'Brien, T. P., Looper, M. D., and Blake, J. B. (2004). Quantification of relativistic
 553 electron microburst losses during the GEM storms. *Geophysical Research Letters*,
 554 31(4). L04802.
- 555 O'Brien, T. P., Lorentzen, K. R., Mann, I. R., Meredith, N. P., Blake, J. B., Fennell,
 556 J. F., Looper, M. D., Milling, D. K., and Anderson, R. R. (2003). Energization of
 557 relativistic electrons in the presence of ULF power and MeV microbursts: Evidence
 558 for dual ULF and VLF acceleration. *Journal of Geophysical Research: Space*
 559 *Physics*, 108(A8).
- 560 Ozaki, M., Miyoshi, Y., Shiokawa, K., Hosokawa, K., Oyama, S.-i., Kataoka, R.,
 561 Ebihara, Y., Ogawa, Y., Kasahara, Y., Yagitani, S., et al. (2019). Visualization of
 562 rapid electron precipitation via chorus element wave–particle interactions. *Nature*
 563 *communications*, 10(1):257.
- 564 Parks, G. K. (1967). Spatial characteristics of auroral-zone X-ray microbursts. *Journal*
 565 *of Geophysical Research*, 72(1):215–226.
- 566 Reeves, G., Spence, H. E., Henderson, M., Morley, S., Friedel, R., Funsten, H., Baker,
 567 D., Kanekal, S., Blake, J., Fennell, J., et al. (2013). Electron acceleration in the
 568 heart of the van allen radiation belts. *Science*, 341(6149):991–994.
- 569 Reeves, G. D., McAdams, K. L., Friedel, R. H. W., and O'Brien, T. P. (2003). Ac-
 570 celeration and loss of relativistic electrons during geomagnetic storms. *Geophysical*
 571 *Research Letters*, 30(10):n/a–n/a. 1529.

- 572 Schulz, M. and Lanzerotti, L. J. (1974). *Particle Diffusion in the Radiation Belts*.
 573 Springer.
- 574 Seppälä, A., Douma, E., Rodger, C., Verronen, P., Clilverd, M. A., and Bortnik, J.
 575 (2018). Relativistic electron microburst events: Modeling the atmospheric impact.
 576 *Geophysical Research Letters*, 45(2):1141–1147.
- 577 Spence, H. E., Blake, J. B., Crew, A. B., Driscoll, S., Klumpar, D. M., Larsen,
 578 B. A., Legere, J., Longworth, S., Mosleh, E., O'Brien, T. P., Smith, S., Springer,
 579 L., and Widholm, M. (2012). Focusing on size and energy dependence of electron
 580 microbursts from the van allen radiation belts. *Space Weather*, 10(11).
- 581 Summers, D. (2005). Quasi-linear diffusion coefficients for field-aligned electro-
 582 magnetic waves with applications to the magnetosphere. *Journal of Geophysical
 583 Research: Space Physics*, 110(A8):n/a–n/a. A08213.
- 584 Summers, D., Thorne, R. M., and Xiao, F. (1998). Relativistic theory of wave-particle
 585 resonant diffusion with application to electron acceleration in the magnetosphere.
 586 *Journal of Geophysical Research: Space Physics*, 103(A9):20487–20500.
- 587 Thorne, R. M., O'Brien, T. P., Shprits, Y. Y., Summers, D., and Horne, R. B. (2005).
 588 Timescale for MeV electron microburst loss during geomagnetic storms. *Journal
 589 of Geophysical Research: Space Physics*, 110(A9). A09202.
- 590 Trefall, H., Bjordal, J., Ullaland, S., and Stadsnes, J. (1966). On the extension of
 591 auroral-zone x-ray microbursts. *Journal of Atmospheric and Terrestrial Physics*,
 592 28(2):225–233.
- 593 Tsurutani, B. T. and Lakhina, G. S. (1997). Some basic concepts of wave-particle
 594 interactions in collisionless plasmas. *Reviews of Geophysics*, 35(4):491–501.
- 595 Ukhorskiy, A. Y., Anderson, B. J., Brandt, P. C., and Tsyganenko, N. A. (2006).
 596 Storm time evolution of the outer radiation belt: Transport and losses. *Journal of
 597 Geophysical Research: Space Physics*, 111(A11):n/a–n/a. A11S03.
- 598 Van Allen, J. A. (1959). The geomagnetically trapped corpuscular radiation. *Journal
 599 of Geophysical Research*, 64(11):1683–1689.
- 600 Vernov, S. and Chudakov, A. (1960). Investigation of radiation in outer space. In
 601 *International Cosmic Ray Conference*, volume 3, page 19.
- 602 Walker, A. D. M. (1993). *Plasma waves in the magnetosphere*, volume 24. Springer
 603 Science & Business Media.